Opto-Electronics Review

Dark current behaviour of type-II superlattice longwave infrared photodetectors under proton irradiation

Clara Bataillon[1*], Jean-Phillipe Perez[1], Rodolphe Alchaar[1], Alain Michez[1], Olivier Gilard[2], Olivier Saint-Pé[3], Philippe Christol[1]

[1]University of Montpellier, 163 Auguste Broussonnet St., 34090 Montpellier, France
[2]CNES, 18 Edouard Belin Ave., 31400 Toulouse, France
[3]Airbus Defense & Space, 31 des Cosmonautes St., 31400 Toulouse, France

Article info	Abstract
	In this work, the authors investigated the influence of proton-irradiation on the dark current of XBp longwave infrared InAs/GaSb type-II superlattice barrier detectors, showing a cut-off wavelength from 11 µm to 13 µm at 80 K. The proton irradiations were performed with 63 MeV protons and fluences up to $8 \cdot 10^{11}$ H$^+$/cm² on a type-II superlattice detector kept at cryogenic (100 K) or room temperature (300 K). The irradiation temperature of the detector is a key parameter influencing the effects of proton irradiation. The dark current density increases due to displacement damage dose effects and this increase is more important when the detector is proton-irradiated at room temperature rather than at cryogenic temperature.

1. Introduction

Today, for space applications, the use of detectors is necessary to identify, track, and determine the status of both cold and hot objects, illuminated or not, very close or very far away. For many of them, high performance infrared (IR) detectors are more and more requested to cover a wide spectral range, from shortwave infrared (SWIR) – 1 to 3 µm and midwave infrared (MWIR) – 3 to 5 µm, to longwave infrared (LWIR) – 8 to 12 µm and very longwave infrared (VLWIR) of $\lambda > 12$ µm. The SWIR and MWIR detectors allow to observe the Earth by studying high temperature-objects while imaging using LWIR and VLWIR devices can detect cold objects in a cold environment, suitable for understanding the universe.

The current material of choice for most high-performance IR detection and space-based applications is mercury/cadmium/telluride (MCT) [1]. But this technology suffers from a relatively low material homogeneity, especially in the LWIR and VLWIR spectral domains.

During the last ten years, an InAs/GaSb type-II superlattice (T2SL) photodetector has emerged as a complementary IR technology to those already well established [2, 3], in particular for space applications by exhibiting an excellent radiometric stability over time [4]. However, the T2SL suffers from a weak Shockley-Read-Hall (SRH)-limited minority carrier lifetime (typically 30 ns in the LWIR [5]), inducing high dark current values. However, the introduction of barrier structure detectors in the late 2000s helps mitigate this drawback [6, 7]. In this structure, an appropriate wide bandgap barrier, inserted between the T2SL absorber layer and the contact layer, blocks majority carriers without impeding the flow of minority carriers. Compared to a standard photodiode, this configuration reduces the detector dark current by confining the electric field inside the barrier, allowing to suppress the generation-recombination (GR) current and to achieve a diffusion-limited performance [8, 9]. Moreover, the barrier can block surface currents (which are considered as a larger detriment than GR currents in III-V technology [6]) arising from the heavily n-type mesa surfaces of these materials.

In the space radiative environment, there are many high energy particles (especially protons) which induce the major problem for the use of electronic components embedded in space systems [10]. The reason determining

*Corresponding author at: clara.bataillon@ies.univ-montp2.fr

the radiation tolerance of an electronic device remains under investigation [11]. Protons are found in different radiation sources like solar winds, cosmic rays, solar eruptions, radiation belts, with proton energy up to 100 MeV. Protons can knock atoms out of their place in the lattice due to the non-ionizing energy loss resulting from an elastic or inelastic scattering of an incoming proton with an atomic nucleus [12]. The displacement of atoms creates vacancy-interstitial pairs and other defects, which damages the carrier lifetime and the dark current in IF detectors due to the SRH mechanism [13]. The displacement damage dose can also be manifested by a modification of the doping level after irradiation, affecting the diffusion dark current [14]. However, protons also induce a total ionizing dose which can cause more damages than the displacement of atoms, but this contribution appears when there is an interface between the dielectric and the semiconductor, which is not the case with the authors' photoresist-protected samples.

Studies of the radiation effects on the dark current and quantum efficiency of T2SL barrier detectors have already been performed at cryogenic temperature [14–21], but to the authors' knowledge, the influence of a T2SL barrier photodetector operating temperature under radiation has never been investigated. In this study, InAs/GaSb XBp LWIR T2SL detectors, exhibiting a 50% cut-off wavelength equal to 11 µm and 13 µm at 80 K, were tested under 60 MeV protons with fluences up to $8 \cdot 10^{11}$ H$^+$/cm^2. The irradiations were performed on a T2SL detector kept at cryogenic (100 K) and room temperature (RT) (300 K) during experiments. In this paper, only the behaviour of the dark current density is studied under proton irradiation.

2. Description of T2SL detector structures and measurement setup

The samples are based on a double heterostructure barrier design with a contact layer made of a heavily n-type doped InAs/GaSb SL, a barrier made of a wide bandgap InAs/AlSb SL, and a lightly p-type-doped InAs/GaSb SL absorber (Fig. 1). The XBp T2SL quantum structure period is composed of 15 monolayers (MLs) of InAs and 7 MLs of GaSb (15/7 structure) for samples A, B, and C, and sample D is made of 17 MLs of InAs and 7 MLs of GaSb (17/7 structure). Details on the selection of these LWIR structures have been reported elsewhere [22, 23].
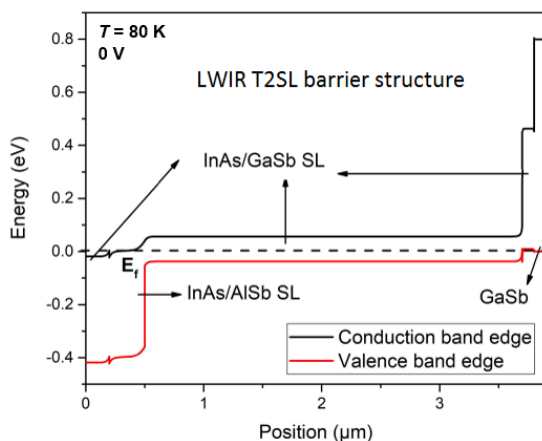
The LWIR T2SL barrier structures have been grown by molecular beam epitaxy (MBE) on n-type (Te-doped) GaSb substrates. Before starting the fabrication process, photoluminescence (PL) measurements were routinely carried out to verify the effective band gap energy of the T2SL absorber layer. Figure 2 shows the PL spectra of all the samples, measured at 80 K. In agreement with the chosen T2SL periods, the samples A, B, C exhibit PL peaks around 11 µm and D shows a PL peak at longer wavelength, close to 13 µm at 80 K.
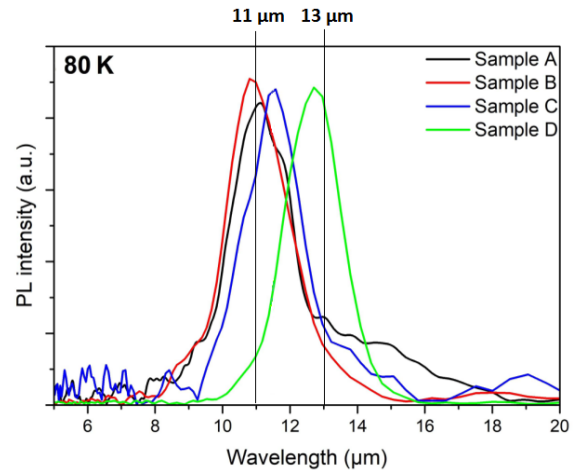
Fig. 2. PL spectra of all samples at 80 K.

After MBE growth, circular mesa photodiodes are fabricated using standard photolithography with a mask set containing blind diodes (C) and photodiodes (P) with several diameters, from 60 µm up to 310 µm. Blind diode is front-side covered by metal; thus, it does not receive any light and may simply be considered as a diode. T2SL photodetectors were then fabricated following a five-step UV photolithography process: Ti/Au top contact deposition by electron beam evaporation; shallow chemical etching of circular mesas with an acid-based solution [23]; protection and electrical insulation of the single pixel device with photoresist polymerized; Ti/Au and AuSn layers deposition, respectively on the contact pads and back-side contact.

The samples were then bonded to a 68-pin lead-free chip carrier (LCC) and mounted into a Janis cryostat to perform non-calibrated spectral photo response (PR) measurements. Figure 3 shows the sample B illuminated from the front side with the spectral PR at different biases and at 80 K. From these curves, the operating bias (V_{op}) can

Fig. 1. Simulated band diagram of the XBp LWIR T2SL barrier structure at 80 K, zero bias and nominal doping conditions. The dashed line represents the Fermi level.
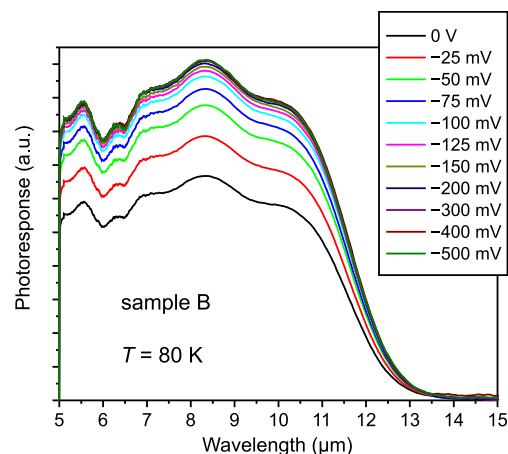
Fig. 3. Sample B: PR measurements at different biases at $T = 80$ K.

be extracted when the PR value saturates. −150 mV will be defined as the V_{op} value. At this bias, a 50% cut-off wavelength close to 11 μm can be extracted, which agrees with the corresponding PL peak (Fig. 2).

Table 1 summarizes the LWIR T2SL detector samples tested with different absorbing layer (AL) thicknesses (1500 nm to 5500 nm) and a different cut-off wavelength (from 11 μm to 13 μm). All these samples are protected by a polymerized photoresist layer and tested under 63 MeV proton irradiation carried out at UCLouvain's Light Ion Facility (UCL-LIF) in Belgium. The proton fluences (Φ_{ph}) were 2, 4, and 8·10^{11} H$^+$/cm^2 and, in order to evaluate the influence of detector temperature during irradiation, two sets of experimental set-ups were planned. For the first set, the detectors were placed in a dedicated cryostat and kept unbiased at 100 K during irradiation. Dark current density-voltage (J-V) measurements were performed after each step of fluence and at 100 K. For the second one, the detectors on LCCs were placed in air at RT (300 K) directly in front of the proton beam with a total proton fluence of 8·10^{11} H$^+$/cm^2. Next, J-V curves were recorded at 100 K, two days after proton irradiation in a probe station.

Table 1.
Summary of the XBp T2SL structures tested under proton radiation.

InAs/GaSb T2SL sample	AL thickness (number of InAs/GaSb periods)	Cut-off wavelength @80 K
A	1500 nm (227 periods)	$\lambda_c = 11$ μm
B	3200 nm (485 periods)	$\lambda_c = 11$ μm
C	5500 nm (833 periods)	$\lambda_c = 11.5$ μm
D	3500 nm (486 periods)	$\lambda_c = 13$ μm

3. Dark current characteristics of samples kept at 100 K during proton irradiation

Figure 4 shows the dark current densities at 100 K of the LWIR T2SL barrier detector (sample B) kept at 100 K during proton irradiation. The green, blue, and red solid lines represent the J-V measurement performed for fluences ranging from 2·10^{11} H$^+$/cm^2 to 8·10^{11} H$^+$/cm^2 [Fig. 4(a)]. The black line is the pre-irradiation measurement performed in the cryostat. Figure 4(b) shows the dark current values extracted at the operating bias $V_{op} = -150$ mV and at the higher bias $V = -500$ mV from J-V characteristics.

Degradation of the dark current was observed with a change in the shape of the J-V curves. The diffusion plateau disappears within the first step of fluence (2·10^{11} H$^+$/cm^2) with an increase of the dark current due to the degradation of the lifetime value [14]. However, the detector dark current remains diffusion-limited after irradiation down to 100 K [23].

In Fig. 4(b), at the operating bias $V_{op} = -150$ mV, the sample B is damaged only by a factor of 2.1 after the last step of proton fluence (8·10^{11} H$^+$/cm^2). Such a weak degradation could be attributed to the barrier design with a high electric field confined in the barrier layer. The dark current increase is not linear with the proton fluence Φ_{ph} and seems to vary in linear-to-square root of Φ_{ph}, corresponding to the dark current dominated by the diffusion current. At a higher bias ($V = -500$ mV), the dark
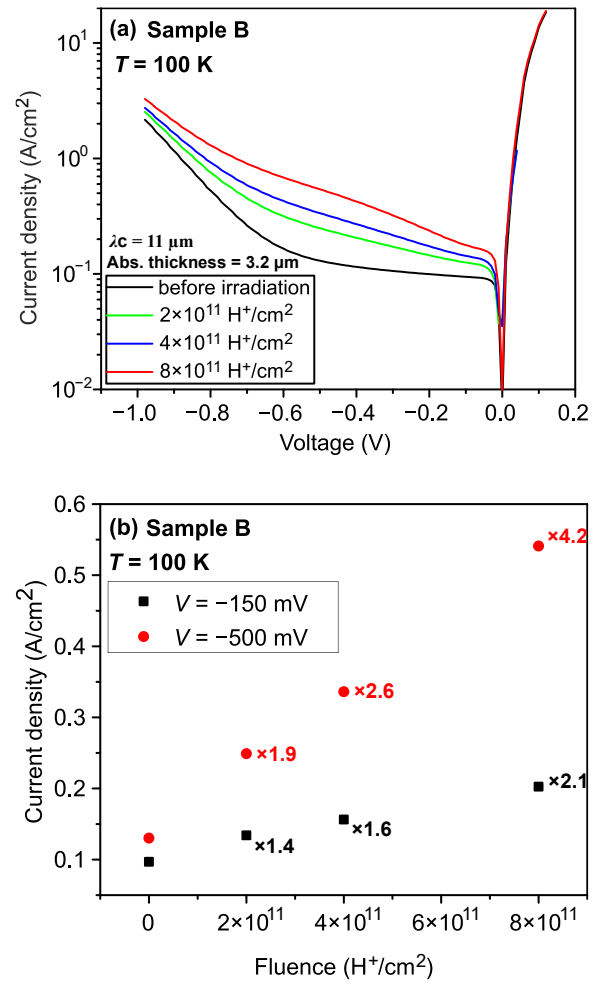
Fig. 4. Sample B J-V characteristics at 100 K and at different proton fluences of the T2SL photodetector irradiated at 100 K (a). The dark current density values extracted at $V = -150$ mV (black points) and $V = -500$ mV (red points) from J-V characteristics performed just after proton irradiation steps (b).

current increases linearly with the proton fluence which implies that the GR current is dominant.

Such a behaviour was observed for all devices of sample B protected with photoresist, both on diodes and photodiodes.

3.1. Influence of absorption layer thickness

In addition to sample B to which AL is made up of 485 periods, two other T2SL devices from samples A and C have been irradiated at 100 K under proton fluence up to 8·10^{11} H$^+$/cm^2. J-V measurements were performed at 100 to observe the influence of AL thickness under radiation.

Figures 5(a) and 5(b) show the dark current density before and after irradiation, for the sample A (227 periods) and sample C (833 periods), respectively. As for sample B, degradation in the dark current was observed for the first step of fluence (2·10^{11} H$^+$/cm^2) and this degradation does not exceed factor 3 at the higher fluence.

To evaluate the possible influence of AL thickness (thus, the number of T2SL periods) on the dark current degradation, the factor J/J_0 (where J_0 stands for the dark current density before radiation) at operating bias was plotted for each proton fluence [Fig. 5(c)]. No significant influence of the number of periods is observed in dark

current degradation, highlighting that the number of interfaces in T2SL quantum structures is not sensitive to proton irradiation.

Moreover, the shape of the dark current damage is clearly different for samples A and B [Fig. 5(c)]. Sample A, which has the smallest absorber width (L_A), is most likely of all the samples to have a diffusion length higher than L_A. Consequently, its dark current damage shows a linear dependence with the proton fluence Φ_{ph} in contrast to

sample B with a linear-to-square root dependence on Φ_{ph}. Sample C has a more similar behaviour as sample B, a slight roll-over, but it also has a slightly longer cut-off wavelength and at the same operating temperature (100 K), and it will have a higher rate of increase than sample B.

3.2. Influence of cut-off wavelength

Other T2SL devices from samples B and D have been irradiated at 100 K under proton fluence up to $8 \cdot 10^{11}$ H+/cm². *J-V* measurements were performed at 100 K to observe the influence of a cut-off wavelength under radiation. Figure 6(a) shows the dark current density before and after irradiation for sample D while the J/J_0 ratio is plotted in Fig. 6(b) to compare samples B and D having the same number of periods for two LWIR different cut-off wavelengths (11 μm *vs*. 13 μm). The dark current degradation seems to be slightly dependent on the LWIR cut-off wavelength, in particular after the last step of proton fluence ($8 \cdot 10^{11}$ H+/cm²). However, such degradation remains comparable to that observed for samples A and C.

According to Morath *et al.* [24], the damage factor decreases when $(\lambda_c T)^{-1}$ increases. Thus, a sample with a higher cut-off wavelength has a higher damage factor. This is coherent with the obtained results displayed in Fig. 6(b). Sample D is more damaged than sample B.
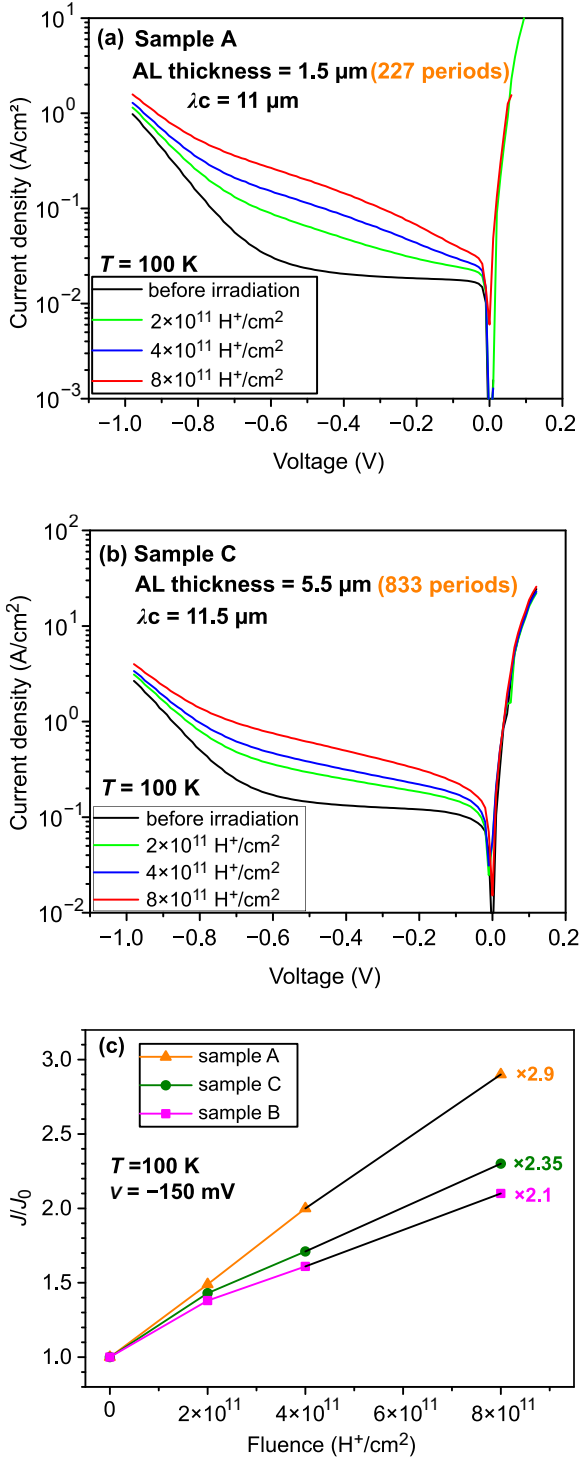
Fig. 5. *J-V* characteristics at 100 K and at different proton fluences of the T2SL detector sample A (a) and sample C (b), irradiated at 100 K. J/J_0 factor extracted at two different bias $V = -150$ mV and $V = -500$ mV from *J-V* characteristics of samples A (227 periods), B (485 periods), and C (833 periods) performed just after proton irradiation steps (c).
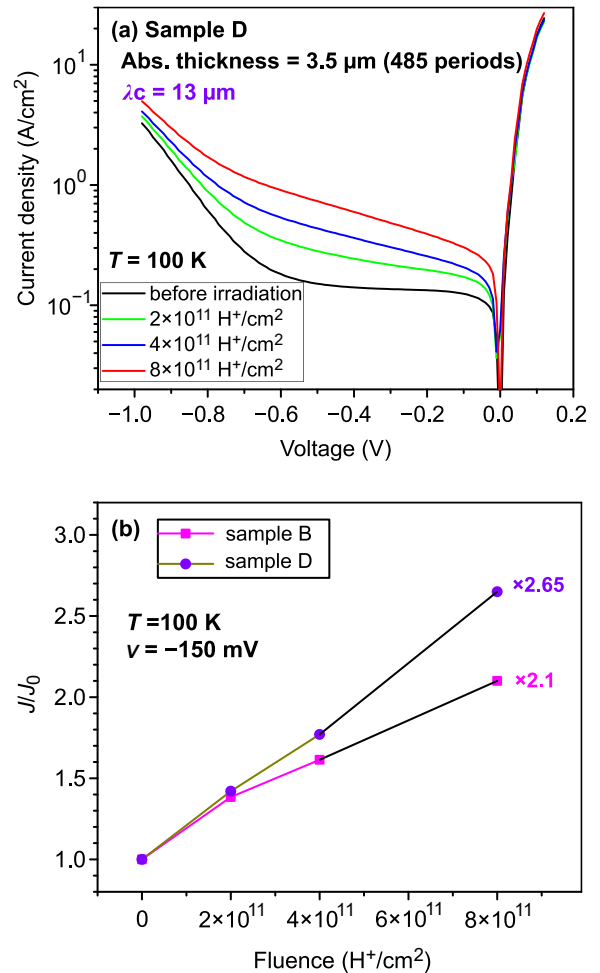
Fig. 6. *J-V* characteristics at 100 K and at different proton fluences of the T2SL detector sample D irradiated at $T = 100$ K (a). J/J_0 factor extracted at operating bias $V = -150$ mV from *J-V* characteristics of samples B and D performed just after proton irradiation steps (b).

3.3. Influence of room temperature annealing

Additional measurements were performed after six months on samples A (227 periods) and C (833 periods), kept at room temperature during this time. Results are shown in Fig. 7(a) and Fig. 7(b), respectively.

A partial recovery of *J-V* curve with a small decrease of the dark current density is observed; however, the diffusion plateau is not recovered. In Fig. 7(c), the J/J_0 ratio is

represented at operating bias $V = -150$ mV, the recovery with annealing is around 25% for both samples. Such behaviour was already observed in III-V nBn infrared detectors [13, 25].

4. Dark current characteristics of samples kept at 300 K during proton irradiation

Devices from samples A and C have also been irradiated at 300 K under a proton fluence equal to $8 \cdot 10^{11}$ H$^+$/cm^2, even if it is not its operating temperature. Next, *J-V* measurements were performed at 100 K.

Figure 8(a) shows the dark current density before and after irradiation for sample A. Compared to Fig. 5(a), sample B is more damaged when the proton irradiation takes place at RT.

From the *J-V* curves recorded before and after the proton fluence of $8 \cdot 10^{11}$ H$^+$/cm^2, the dark current values were extracted at -150 mV and plotted against the perimeter (P) to area (A) ratio in Fig. 8(b). An overall degradation by factor 7 can be observed. Regardless of their size, photodiodes and blind diodes were damaged in a similar way, evidencing no size-dependence, and indicating the absence of surface leakage current for these devices protected by a polymerized photoresist layer.

Fig. 7. *J-V* characteristics at 100 K after the last proton fluence ($8 \cdot 10^{11}$ H$^+$/cm^2) and measurement after six months, at RT, for samples A (a) and C (b), J/J_0 factor extracted at operating bias $V = -150$ mV from *J-V* characteristics of samples A and C performed just after the proton irradiation steps and after six months at RT (c).
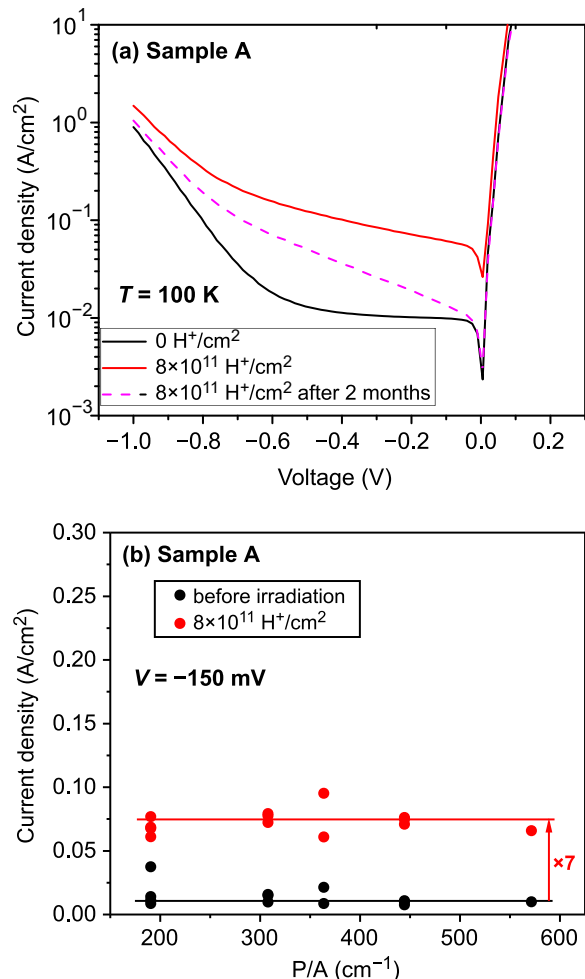
Fig. 8. In solid line, dark current density-voltage (*J-V*) characteristics at 100 K and at different proton fluences of sample A irradiated at 300 K. In dashed line, *J-V* curves after two months of room temperature annealing (a), dark current density as a function of P/A ratio extracted at $V = -150$ mV (b).

Additional *J-V* measurements have been done after two months to observe any potential room temperature annealing. A partial recovery of the dark current density value is observed after 2 months. However, the device has not recovered its diffusion plateau and remains current-limited GR despite the improvement in dark current density.

Figure 9 displays the dark current density before and after irradiation for the sample C having the widest AL (5500 nm thick). The results show, once again, no dependence on the T2SL period. Indeed, a similar behaviour to that of sample A is observed both for the overall dark current degradation and for the partial recovery of the dark current after a few days of RT annealing. This incomplete recovery of the dark current, already observed in Ref. 26, is attributed to displacement damage.
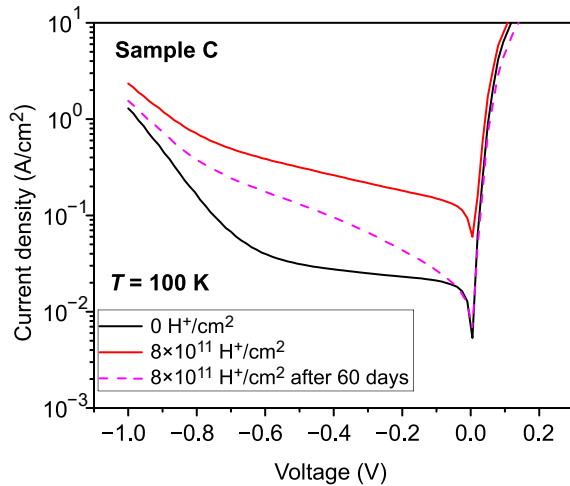
Fig. 9. In solid line, *J-V* characteristics at 100 K and at different proton fluences of sample C irradiated at 300 K. In dashed line, *J-V* curves after two months of RT annealing.

5. Influence of the detector temperature under proton irradiation

In this section, a comparison of the dark current density degradation when the detector is kept at 100 K and 300 K during irradiation is presented (Fig. 10). In both cases, the samples are proton-irradiated, with a fluence of $8 \cdot 10^{11}$ H$^+$/cm².
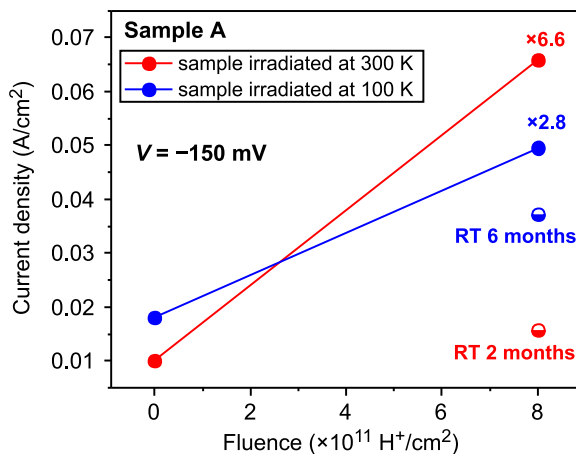
Fig. 10. *J-V* measurements values after $8 \cdot 10^{11}$ H$^+$/cm² proton fluence of the detector irradiated at 300 K (red lines) and at 100 K (blue lines) at the operating bias $V = -150$ mV. The half-coloured symbols represent the corresponding measurements after 2 months and 6 months at RT.

The damage of the dark current density is more important when the detector is irradiated at RT (300 K). At the operating bias $V = -150$ mV, the dark current density value is multiplied by factor 2.8 when the detector is irradiated at 100 K and by factor 6.4 when it is irradiated at 300 K. The detectors were then kept at RT. After 2 months, the sample irradiated at 300 K recovers 70% of the initial dark current density value against 25% (after six months) when the sample is irradiated at 100 K. The RT annealing induces a partial recovery of the dark current. This recovery is higher when the detector temperature during irradiation is 300 K. However, it should be noted that the dark current densities do not recover their initial values [26].

6. Conclusions

XBp InAs/GaSb LWIR T2SL detectors were proton-irradiated with a proton energy equal to 63 MeV and a fluence up to $8 \cdot 10^{11}$ H$^+$/cm².

When the detector is irradiated at 100 K, the dark current density degrades by factor 2–3, regardless of the thickness of the absorbing layer, therefore (and subsequently the number of T2SL periods), and irrespective of the cut-off wavelength in the LWIR domain. Measuring the dark current density after each fluence allowed the authors to show that the current behaviour was no longer diffusion-limited even after the first irradiation. Thermal annealing at RT for 6 months induced a partial recovery of the electrical performance of the devices, but they did not recover the diffusion-limited behaviour of the dark current.

Degradation is at least two times higher when the detector is irradiated at 300 K, but under RT annealing, the partial recovery of the dark current is better without limiting the diffusion of the dark current.

These measurements highlight the importance of the temperature detector during proton irradiation that induces different mechanisms of degradation. Thus, to better understand these degradation mechanisms under irradiation, the technology computer-aided design (TCAD) modelling will be the subject of the forthcoming studies.

References

[1] Minoglou, K. *et al.* Infrared image sensor developments supported by the European Space Agency. *Infrared Phys. Technol.* **96**, 351–360 (2019). https://doi.org/10.1016/j.infrared.2018.12.010

[2] Rogalski, A., Martyniuk, P. and Kopytko, M. InAs/GaSb type-II superlattice infrared detectors: Future prospect. *Appl. Phys. Rev.* **4**, 031304 (2017). https://doi.org/10.1063/1.4999077

[3] Razeghi, M. *et al.* Antimonide-based type II superlattices: a superior candidate for the third generation of infrared imaging systems. *J. Electron. Mater.* **43**, 2802–2807 (2014). https://doi.org/10.1007/s11664-014-3080-y

[4] Arounassalame, V. *et al.* Robust evaluation of long term stability of an InAs/GaSb type II superlattice midwave infrared focal plane array. *IEEE Trans. Instrum. Meas.* **70**, 1–8 (2021). https://doi.org/10.1109/TIM.2020.3024406

[5] Donetsky, D., Belenky, G., Svensson, S. & Suchalkin, S. Minority carrier lifetime in T2SL InAs-GaSb strained layer superlattice and bulk HgCdTe materials. *Appl. Phys. Lett.* **97**, 052108 (2010). https://doi.org/10.1063/1.3476352

[6] Maimon, S. & Wicks, G. W. nBn detector, an infrared detector with reduced dark current and higher operating temperature. *Appl. Phys. Lett.* **89**, 151109 (2006). https://doi.org/10.1063/1.2360235

[7] Klipstein, P. C. XBn barrier photodetectors for high sensitivity and high operating temperature infrared sensors. *Proc. SPIE* **6940**, 69402U (2008). https://doi.org/10.1117/12.778848

[8] Klipstein, P. C. XBnn and XBpp infrared detectors. *J. Cryst. Growth* **425**, 351–356 (2015). https://doi.org/10.1016/j.jcrysgro.2015.02.075

[9] Delmas, M., Rossignol, R., Rodriguez, J.-B. & Christol, P. Design of InAs/ GaSb superlattice infrared barrier detectors. *Superlattices Microstruct.* **104**, 402–414 (2017). https://doi.org/10.1016/j.spmi.2017.03.001

[10] Logan, J. V., Short, M. P., Webster, P. T. & Morath, C. P. Orbital equivalence of terrestrial radiation tolerance experiments. *IEEE Trans. Nucl. Sci.* **67**, 2382–2391 (2020). https://doi.org/10.1109/TNS.2020.3027243

[11] Logan, J. V. *et al.* Understanding the fundamental driver of semiconductor radiation tolerance with experiment and theory. *Phys. Rev. Mater.* **6**, 084601 (2022). https://doi.org/10.1103/PhysRevMaterials.6.084601

[12] W. de Boer, J. *et al.* Radiation hardness of diamond and silicon sensors compared. *Phys. Stat. Sol. A* **204**, 3004–3010 (2007). https://doi.org/10.1002/pssa.200776327

[13] Jenkins, G. D., Morath, C. P. & Cowan, V. M. Empirical study of the disparity in radiation tolerance of the minority-carrier lifetime between II-VI and III-V MWIR detector technologies for space applications. *J. Electron. Mater.* **46**, 5405–5410 (2017). https://doi.org/10.1007/s11664-017-5628-0

[14] Morath, C. P., Garduno, E. A, Jenkins, G. D. Steenbergen, E. A. & Cowan, V. M. Effects of 63 MeV proton-irradiation on the dark-current in III-V-based, unipolar barrier infrared detectors. *Infrared Phys. Technol.* **97**, 448–455 (2019). https://doi.org/10.1016/j.infrared.2018.12.033

[15] Jackson, E. M. *et al.* Radiation damage in type ii superlattice infrared detectors. *J. Electron. Mater.* **39**, 852–856 (2010). https://doi.org/10.1007/s11664-010-1227-z

[16] Cowan, V. M. *et al.* Radiation tolerance characterization of dual band InAs/GaSb type-II strain-layer superlattice pBp detectors using 63 MeV protons. *Appl. Phys. Lett.* **101**, 251108 (2012). https://doi.org/10.1063/1.4772543

[17] Soibel, A. *et al.* Proton radiation effect on performance of InAs/GaSb complementary barrier infrared detector. *Appl. Phys. Lett.* **107**, 261102 (2015). https://doi.org/10.1063/1.4938756

[18] Morath, C. P., Garduno, E. A., Cowan, V. M. & Jenkins, G. D. More accurate quantum efficiency damage factor for proton-irradiated, III-V-based unipolar barrier infrared detectors. *IEEE Trans. Nucl. Sci.* **64**, 74–80 (2017). https://doi.org/10.1109/TNS.2016.2634500

[19] Hubbs, J. E. Proton radiation experimental results on a III-V nBn mid-wavelength infrared focal plane array. *Proc. SPIE* **9933**, 993307 (2016). https://doi.org/10.1117/12.2240199

[20] Soibel, A. *et al.* Radiation tolerance studies of long wavelength infrared InAs/GaSb detectors. *Proc. SPIE*, **9755**, 975511 (2016). https://doi.org/10.1117/12.2209187

[21] Höglund, L. *et al.* Influence of proton radiation on the minority carrier lifetime in midwave infrared InAs/InAsSb superlattices. *Appl. Phys. Lett.* **108**, 263504 (2016). https://doi.org/10.1063/1.4954901

[22] Höglund, L. *et al.* Influence of shallow versus deep etching on dark current and quantum efficiency in InAs/GaSb superlattice photodetectors and focal plane arrays for long wavelength infrared detection. *Infrared Phys. Technol.* **95**, 158–163 (2018). https://doi.org/10.1016/j.infrared.2018.10.036

[23] Alchaar, R., Rodriguez, J.-B., Höglund, L., Naureen, S. & Christol, P. Characterization of an InAs/GaSb type-II superlattice barrier photodetector operating in the LWIR domain. *AIP Adv.* **9**, 055012 (2019). https://doi.org/10.1063/1.5094703

[24] Morath, C. P., Cowan, V. M., Treider, L. A., Jenkins, G. D. & Hubbs, J. E. Proton irradiation effects on the performance of III-V-based unipolar barrier infrared detectors. *IEEE Trans. Nucl. Sci.* **62**, 512–519 (2015). https://doi.org/10.1109/TNS.2015.2392695

[25] Morath, C. P., Steenbergen, E. H., Jenkins, G. D., Hubbs, J. E. &. Maestas, D. Irradiation effects on the performance of III-V-based nBn infrared detectors. *J. Radiation Effects* **38**, 161–170 (2020). https://apps.dtic.mil/sti/pdfs/AD1093146.pdf

[26] Steenbergen, E. H. *et al.* A recent review of mid-wavelength infrared type-II superlattices: carrier localization, device performance, and radiation tolerance. *Proc. SPIE* **10111**, 1011104 (2017). https://doi.org/10.1117/12.2266040